Infrared Thermophotonics: Theoretical benchmarking of Ni–Al superalloys

Thien Duc Ngo, Hai Dang Ngo, Toan Phuoc Tran, Hiroshi Harada, and Tadaaki Nagao**

T. D. Ngo, H. D. Ngo, T. P. Tran, T. Nagao
Research Center for Materials Nanoarchitectonics (MANA), National Institute for Materials Science (NIMS), 1-1 Namiki, Tsukuba, Ibaraki 305-0044, Japan
Email: DucThien.NGO@nims.go.jp; NAGAO.Tadaaki@nims.go.jp

T. D. Ngo, H. D. Ngo, T. P. Tran, T. Nagao
Department of Condensed Matter Physics, Graduate School of Science, Hokkaido University, Kita 10, Nishi 8, Kita-ku, Sapporo 060-0810, Japan

H. Harada
Distinguished Emeritus Researcher, National Institute for Materials Science (NIMS), 1-2-1 Sengen, Tsukuba, Ibaraki 305-0047, Japan

Keywords: high-temperature superalloys, intermetallics, nickel–aluminium, thermophotonics, thermal emitters

Abstract

Ni–Al intermetallic compounds are highly stable, heat-resistant superalloys that have been studied as possible materials for automotive and aerospace applications. However, no reports of their thermophotonic applications, such as high-temperature IR emitters, have been reported. Herein, we report an integrated approach that combines a theoretical investigation of the optical properties of Ni–Al compounds with an optimized geometrical microdevice design. Benchmarking of the optical properties and device performance revealed that NiAl exhibited the best optical properties among the surveyed families of Ni–Al intermetallic compounds, comparable to those of conventional plasmonic materials in the IR region. Additionally, the NiAl-based microdevices exhibited an excellent quality of 692, making them promising high-temperature plasmonic superalloys for IR thermophotonic applications. In addition, the experimental dielectric function in the IR region was consistent with the simulated value. Simultaneously, we successfully modeled various designs of plasmonic metamaterial

structures based on NiAl, demonstrating the good performance of this material as a perfect spectroscopic absorber and emitter operating in the IR region.

1. Introduction

In recent years, interest in the development of IR nano/microdevices to control thermal radiation and meet sustainable development goals (SDGs) has increased, particularly in terms of enhancing energy efficiency and cost-effectiveness. Key performance factors include the choice of the optimum plasmonic material and the surface nano/microstructure design. Although noble metals and base metals such as Al are suitable plasmonic elements for applications in the UV–vis or IR regions,[1–3] their role in photothermal applications is limited because of their low thermal stability and inherent ohmic and collisional losses in the IR region.[4–6] Expanding studies on plasmonic thin-film materials beyond the abovementioned elemental metals to novel high-temperature superalloys has the potential to achieve thermally stable materials with excellent spectral tunability. This is significant for the practical applications of these materials and devices, particularly in harsh chemical environments and at high temperatures.

In this study, we investigated Ni–Al intermetallic compounds as thermally stable plasmonic building blocks for IR photothermal applications. Ni- or Al-based superalloys are thermally stable, heat-resistant materials that have been widely employed in automobile and aviation technologies.[7][8–11] Among them are nickel–aluminum intermetallic compounds, promising superalloys with extremely high melting points (> 1400 °C),[12] which are materials of choice for aircraft engine components, such as high-pressure turbine blades. In the form of thin films, Ni–Al intermetallic compounds have also been studied as barrier coatings. Previous atomic-level research on Ni–Al intermetallic compounds comprehensively examined their crystal and electronic structures, mechanical properties, and thermodynamics;[13–18] some early studies also investigated the optical properties of these compounds.[19–26] Moreover, several studies have focused on crystal growth and thin-film deposition.[27–30] However, no studies have focused on their thermophotonic properties and potential IR device applications, such as perfect plasmonic absorbers, thermal emitters, molecular sensors, and thermophotovoltaics. To enable research in this unexplored field, we used Kohn–Sham density functional theory (DFT) calculations and Maxwellian electromagnetic (EM) design optimization to develop microdevices based on Ni–Al intermetallic compounds for high-temperature IR applications.[31,32] First, DFT calculations were employed to investigate the chemical compositions, crystal structures, and optical properties of the Ni–Al compounds. The candidates that exhibited the best optical properties were chosen for experimental characterization, including X-ray diffraction (XRD), electrical properties, and dielectric function measurements. The experimental results were compared with those obtained theoretically. Second, electromagnetic microdevice optimization was performed to determine the design of IR microdevices. We also examined the "material–device relationship" of the Ni–Al intermetallic compounds by benchmarking the microdevice performance and selected NiAl as the best material among the candidate Ni–Al compounds. Additionally, we benchmarked both the optical properties of NiAl and the performance of its microdevices against other well-known metals to highlight the potential of NiAl as a replacement for conventional plasmonic materials. Finally, NiAl-based thermophotonic microdevices were simulated and demonstrated. We examined their suitability as perfect IR absorbers, molecular sensors, and high-temperature thermal emitters.

2. Results and Discussion

2.1. Crystal structures and optical properties of Ni–Al intermetallic compounds

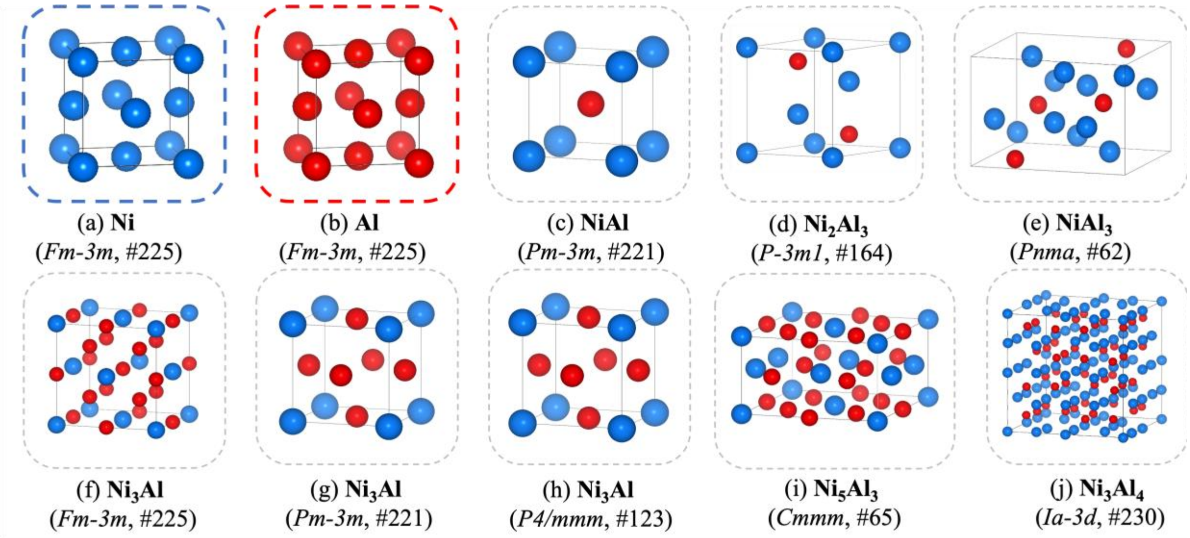

Figure 1. Optimized conventional unit cells of pure bulk (a) Ni and (b) Al, along with their Ni–Al intermetallic compounds (c–j), which have been experimentally observed in different space groups. The intermetallic compounds include (c) NiAl (#221), (d) Ni_2Al_3 (#164), (e)

$NiAl_3$ (#62), (f) Ni_3Al (#225), (g) Ni_3Al (#221), (h) Ni_3Al (#123), (i) Ni_5Al_3 (#65), and (j) Ni_3Al_4 (#230). Blue and red spheres represent Ni and Al atoms, respectively.

First, the crystal structures of the Ni–Al intermetallic compounds were collected from the Inorganic Crystal Structure Database (ICSD) and the Materials Project as initial geometrical inputs for DFT calculations. [37][38][44] Conventional cells of Ni–Al intermetallic compounds that crystallize in various space groups are shown in **Figure 1**. These structures exhibit distinct atomic arrangements based on their stoichiometry and phase, which influence their electronic and optical properties. The atomic structures of pure bulk Ni (**Figure 1(a))** and Al (**Figure 1(b))** are also presented, highlighting the differences in crystal symmetry and atomic packing between the elemental metals and their intermetallic compositions. The optimized lattice constants and cell volumes with respect to the PBE of NiAl are listed in **Table 1**. The values in parentheses are the experimental measurements of the lattice constant and volume columns. With the exception of Ni_3Al (*P*4/*mmm*, #123), which had a volume deviation of 4% from the reference, the remaining compounds had volume deviations of less than 1%. Therefore, the structural parameters are consistent with the reported experimental and calculated results. Among these Ni–Al intermetallic compounds, Ni_3Al (*Pm*-3*m*, #221) and Ni_3Al (*P*4/*mmm*, #123) exhibited magnetic moments, which are consistent with the observations of Min et al.[45] No magnetic moment was observed for any of the remaining compounds. However, further studies on the magnetic properties of these compounds are beyond the scope of this study.

Table 1. Materials, space groups, lattice constants, and volumes of two pure Ni and Al bulks, as well as their compositions in Ni–Al intermetallic compounds, both simulated and experimental.

Material (Identified code)	Space group	Lattice constants [Å]	Volume [$Å^3$]	Ref.
Ni	*Fm-3m (#225)*	3.578, 3.578, 3.578	45.800	[46]
(ICSD 37502)		(3.504, 3.504, 3.504)	(43.040)	
Al	*Fm-3m (#225)*	4.049, 4.049, 4.049	66.400	[47]
(ICSD 18839)		(4.039, 4.039, 4.039)	(65.910)	
NiAl	*Pm*-3*m* (#221)	2.886, 2.886, 2.886	24.037	[48]
(ICSD 191110)		(2.885, 2.885, 2.885)	(24.010)	
Ni_2Al_3	*P*-3*m*1 (#164)	4.032, 4.032, 4.901	69.001	[48]
(ICSD 191103)		(4.036, 4.036, 4.896)	(69.060)	
$NiAl_3$	*Pnma* (#62)	6.610, 7.378, 4.812	234.679	[49]
(ICSD 608787)		(6.598, 7.352, 4.802)	(232.94)	
Ni_3Al	*Fm*-3*m* (#225)	5.654, 5.654, 5.654	180.722	[44]
(MP-672232)		(5.658, 5.658, 5.658)	(181.088)	
Ni_3Al	*Pm*-3*m* (#221)	3.556, 3.556, 3.556	44.951	[50]
(ICSD 608811)		(3.566, 3.566, 3.566)	(45.350)	
Ni_3Al	*P*4/*mmm* (#123)	3.556, 3.556, 3.554	44.951	[49]
(ICSD 107862)		(3.780, 3.780, 3.280)	(46.870)	
Ni_5Al_3	*Cmmm* (#65)	7.454, 6.653, 3.753	186.078	[48]
(ICSD 191113)		(7.554, 6.522, 3.789)	(186.670)	
Ni_3Al_4	*Ia*-3*d* (#230)	11.397, 11.397, 11.397	1480.376	[51]
(ICSD 58042)		(11.408, 11.408, 11.408)	(1484.67)	

The primary objective of this study was to investigate and evaluate the optical properties of Ni–Al intermetallic compounds, particularly in the IR region. The Drude model was used to predict the optical properties of the compounds, for which the plasma frequency and scattering rate were the key parameters, as given by **Equation (2)**. The plasma frequencies of the Ni–Al compounds were calculated from the band structures using **Equation (3)**, and the values obtained are presented in **Table 2** along three coordinates. Owing to the isotropic natures of NiAl (P*m*-3*m*, #221), Ni_3Al (F*m*-3*m*, #225), Ni_3Al (P*m*-3*m*, #221), and Ni_3Al_4 (*Ia*-3*d*, #230), which crystallize in cubic space groups, the same plasma frequencies along the three primary coordinates are exhibited. In contrast, Ni_2Al_3 (*P*-3*m*1, #164), $NiAl_3$ (*Pnma*, #62), Ni_3Al (*P*4/*mmm*, #123), and Ni_4Al_3 (*Cmmm*, #65) have anisotropic structures where the three lattice constants are not equal and the plasma frequencies along the three primary coordinates differ for these materials. We selected the highest plasma frequency for each material to compare the optical properties of the compounds fairly. The plasma frequencies and dielectric functions of pure Ni and Al, as reported by Rakić et al.,[52] are included for reference and comparison with their respective intermetallic compounds, utilizing the same Drude-Lorentz model.

Table 2. Calculated plasma frequencies (ω_p) along the *x*-, *y*-, *z*-directions of Ni–Al intermetallic compounds compared with values for pure Ni and Al reported in literature.

Material	Space group	Crystal system	ω_p (*xx*) [eV]	ω_p (*yy*) [eV]	ω_p (*zz*) [eV]
Ni[a)]	*Fm-3m (#225)*	Cubic	**15.92**	**15.92**	**15.92**
Al[a)]	*Fm-3m (#225)*	Cubic	**14.98**	**14.98**	**14.98**
NiAl	*Pm*-3*m* (#221)	Cubic	**7.143**	**7.143**	**7.143**
Ni_2Al_3	*P*-3*m*1 (#164)	Trigonal	**5.679**	5.679	4.455
$NiAl_3$	*Pnma* (#62)	Orthorhombic	4.579	**5.290**	4.624
Ni_3Al	*Fm*-3*m* (#225)	Cubic	**4.385**	**4.385**	**4.385**
Ni_3Al	*Pm-3m* (#221)	Cubic	**4.262**	**4.262**	**4.262**
Ni_3Al	*P*4/*mmm* (#123)	Tetragonal	4.261	4.261	**4.268**
Ni_5Al_3	*Cmmm* (#65)	Orthorhombic	**4.227**	3.371	4.049
Ni_3Al_4	*Ia*-3*d* (#230)	Cubic	**3.330**	**3.330**	**3.330**

[a)] Taken from literature.[52]

Figure 2 illustrates the calculated total dielectric functions of the Ni–Al intermetallic compounds compared with those of pure Ni and Al. The real part of the dielectric function (ε_1), a quantity that describes the optical response, is illustrated in **Figure 2(a)**. Among the Ni–Al compounds, NiAl (*Pm*-3*m*, #221) (red curve) yielded the largest negative value, indicating the best optical response. In contrast, Ni_3Al_4 (*Ia*-3*d*, #230) exhibits the worst optical properties. The quantity describing the imaginary parts of the optical loss is illustrated in **Figure 2(b)**.

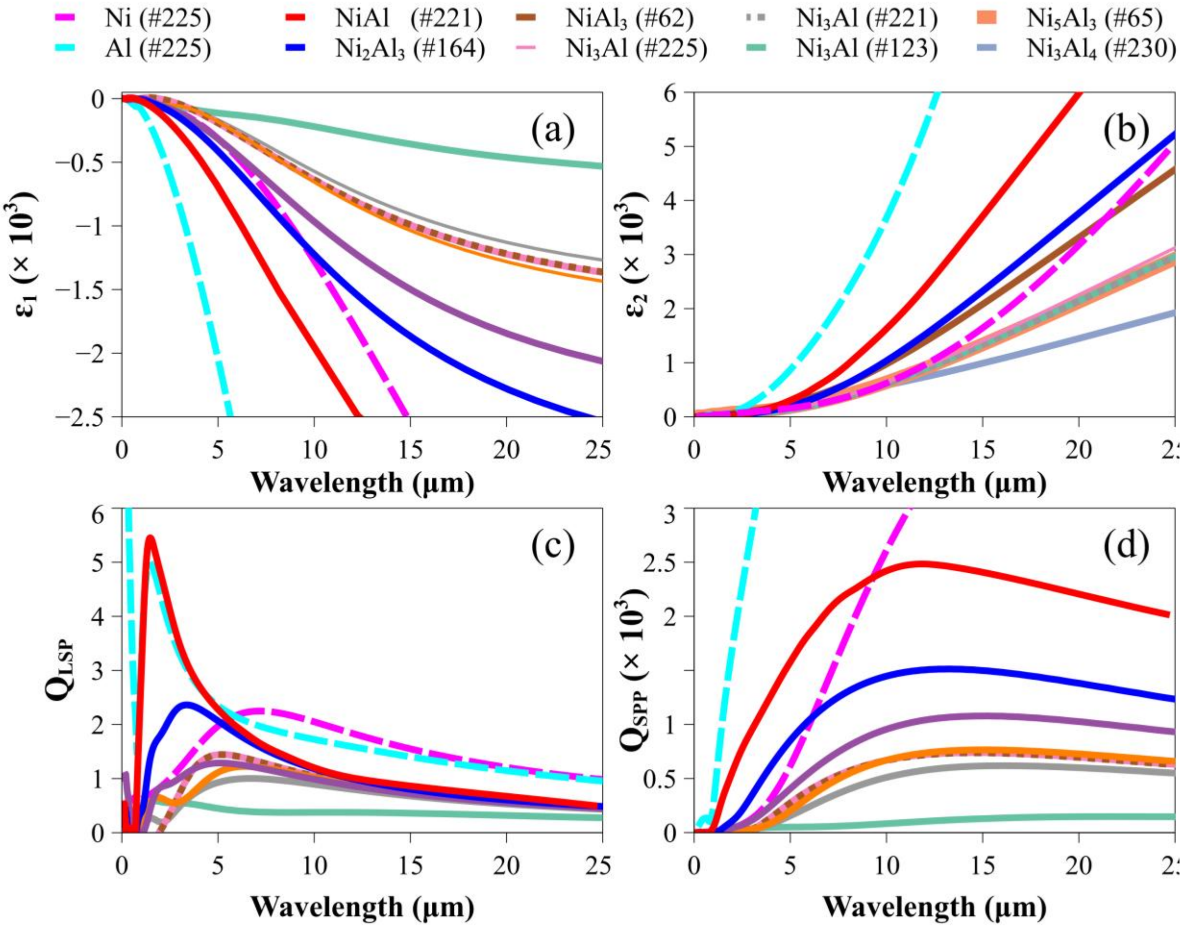

Figure 2. (a) Calculated real and (b) imaginary parts of the total dielectric functions (including interband and intraband transitions) for eight Ni–Al intermetallic compounds, compared with values for pure Ni and Al reported in literature. (c) Q_{LSP} and (d) Q_{SPP} figures-of-merits, providing a comparative analysis of their optical performance.

Ideally, a plasmonic material should have a high optical response (large negative real part) and low optical loss (small imaginary part). Therefore, two figures-of-merit (FOMs), Q_{LSP} (quality factor for localized surface plasmon; $Q_{LSP} = -\varepsilon_1/\varepsilon_2$) and Q_{SPP} (quality factor for surface plasmon polariton; $Q_{SPP} = \varepsilon_1^2/\varepsilon_2$), which are frequently used in the plasmonic research community, were used for the comparison of the plasmonic materials. **Figures 2(c)** and **2(d)** illustrate the Q_{LSP} and Q_{SPP} values of the Ni–Al intermetallic compounds, respectively, compared with those of pure Ni and Al. With respect to the FOMs, NiAl (*Pm*-3*m*, #221) was consistently the best material for the compounds in this study. Therefore, based on the predicted optical properties, NiAl (*Pm*-3*m*, #221) was expected to exhibit the best performance among the Ni–Al compounds. Moreover, in comparison with the elemental metals Ni and Al, the Q_{LSP} of Al is exceptionally high in the UV–vis region. However, the near- and mid-IR regions are comparable to those of NiAl and exhibit the same orders of magnitude. In addition, the Q_{LSP} of NiAl surpassed that of Ni in the IR region by approximately 5 μm, and the Q_{SPP} of NiAl exceeded that of Ni by approximately 8 μm. These results indicate that the optical properties of NiAl are comparable to those of pure Ni and Al. Notably, owing to its high melting point, NiAl can be utilized under high-temperature conditions where Ni and Al may not be suitable. In this context, NiAl (*Pm*-3*m*, #221) was selected as the most promising candidate, and its superior thermophotonic performance was verified by designing an IR microdevice.

2.2. Comparison of DFT results with experimental data from single-crystal NiAl

For verification, we compared the theoretical lattice constant and electrical and optical properties of NiAl with the experimental results. Before characterizing the electrical and optical properties, we determined the crystal structure of the single-crystal NiAl using XRD.

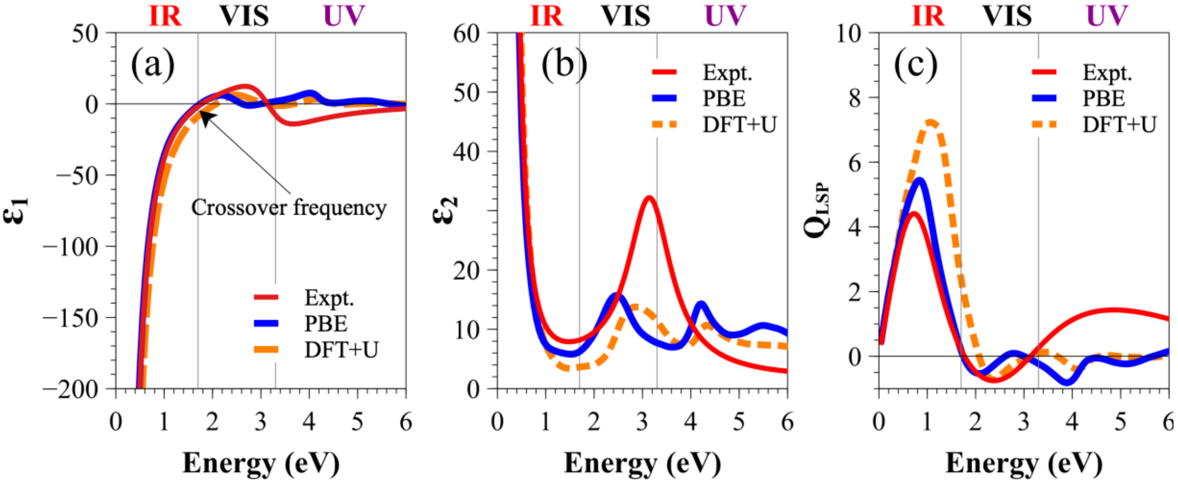

Figure 3. (a) Calculated and experimental real and (b) imaginary parts and (c) FOMs of the total dielectric functions. Vertical grey lines separate three distinct regions: IR ($\varepsilon < 1.7$ eV), VIS ($1.7 \text{ eV} < \varepsilon < 3.3$ eV), and UV ($\varepsilon > 3.3$ eV).

Figure 3 illustrates the simulated and measured dielectric functions of the NiAl single crystal in the photon energy range (0–6 eV). The total dielectric function of NiAl is a combination of the interband and intraband parts, as mentioned in Section 4. The blue line represents the total dielectric function. The total dielectric functions calculated using the DFT + U approximation are plotted for comparison (orange dashed line). The experimental dielectric function fitted with the Drude–Lorentz model is indicated by the solid red line. **Figure 3(a)** illustrates the real part (ε_1) of the dielectric function. The crossover energy (screened plasma energy), which is defined as the photon energy at which $\varepsilon_1 = 0$, where the material starts to exhibit metallic behavior, is shown in Figure 3(a) at 1.74 eV (λ = 711 nm) in the near-IR region. However, in the simple IPA framework and standard PBE approach, the spin-orbit, local-field, and quasiparticle effects were not included. This causes a deviation of approximately 0.5 eV in the peak positions in the visible-to-UV range.[53] This problem can be solved using advanced approaches such as DFT + U, HSE06,[46][47] or Green's function screening (GW) approximation.[56] In the DFT+U framework, the Hubbard *U parameter* can be tuned until the imaginary peak matches the experimental peak. For example, in **Figure 3(b)**, there is an experimental peak at 3.14 eV for the imaginary part. Using the standard PBE functional, the simulated value was 2.46 eV, when U = 6.4 eV for the Ni d-orbital, a peak at 2.88 eV, which is close to the observed peak at 3.14 eV, was observed. However, in the IR region of interest, where intraband excitations dominate the dielectric function, the standard DFT approach and IPA model yield good agreement with the experimental values and are computationally economical.[31,32,53] In **Figure 3(c)**, the strong consistency between the simulated and experimental results for the real and imaginary parts of the IR region indicates that Q_{LSP} exhibits a strong correlation in the corresponding wavelength range.

Table 3. Lattice constants, plasma frequencies, scattering rates, screened plasma wavelengths, and maximum FOM of crystalline NiAl; both simulated and experimental results are shown.

	PBE	DFT + U	Expts.
Lattice constant [Å]	2.886	2.860	2.885[a)], 2.890[b)]
Volume [Å^3]	24.037	23.400	24.013[a)], 24.138[b)]
Plasma frequency [eV]	7.14	8.02	7.49[b)]
Scattering rate [eV]	0.1	0.1	0.12[b)]
Electrical conductivity [$10^7\ \Omega^{-1}\,\mathrm{m}^{-1}$]	0.69	0.87	0.66[b)], 1.0[c)], 1.02[d)]
Screened plasma wavelength [nm]	711	599	700[b)]
Max Q_{LSP}	5.3	7.1	4.3[b)]

[a)] Taken from literature.[48]

[b)] This study.

[c)] Taken from literature.[13]

[d)] Taken from literature.[57]

Table 3 lists a comparison of the physical parameters of NiAl calculated using first-principles DFT with the experimental values. The volume calculated using DFT + U is slightly lower than the experimental value (2.6%) (Table 3). We also estimated the experimental plasma frequency, scattering rate, and conductivity of single-crystal NiAl using ellipsometry, finding

7.49 eV, 0.12 eV, and $0.66 \times 10^7\ \Omega^{-1}\ \mathrm{m}^{-1}$, respectively. Our experimental scattering rate matches the empirical estimated value ($\gamma = 0.1$ eV) well. Notably, the PBE functional provided results closer to the experimental values, particularly for the lattice constant and plasma frequency. The DFT + U formalism can improve the exchange-correlation and interband dielectric functions; however, it does not significantly affect the dielectric function in the IR region, where the intraband contribution dominates the total dielectric function. Therefore, in this study, we used the dielectric function obtained at the PBE level for IR microdevice optimization for thermophotonic applications in the IR region.

2.3. Proposed high-temperature Ni–Al intermetallic thermophotonic microdevices

As heat-resistant and thermally stable candidate materials, Ni–Al intermetallic materials have high-temperature applications such as high-pressure turbine blades and aircraft engine components, as described earlier. According to Kirchhoff's law of thermal equilibrium,[58] the emissivity is equivalent to the absorptivity. Therefore, the absorptivity of the devices can be simulated to assess the performance of IR emitters and absorbers. We expect that Ni–Al compounds can be used in IR applications, especially as high-temperature thermal emitters. First, we examined the relationship between the optical properties of the candidate materials and the absorptivity of their IR microdevices, focusing on the grating-type absorber structure. Subsequently, the optimal candidate was used to design typical microdevices for the absorbers and thermal emitters.

2.3.1. Benchmarking the photothermal performance of microdevices prepared with different Ni–Al intermetallic compounds and conventional plasmonic materials

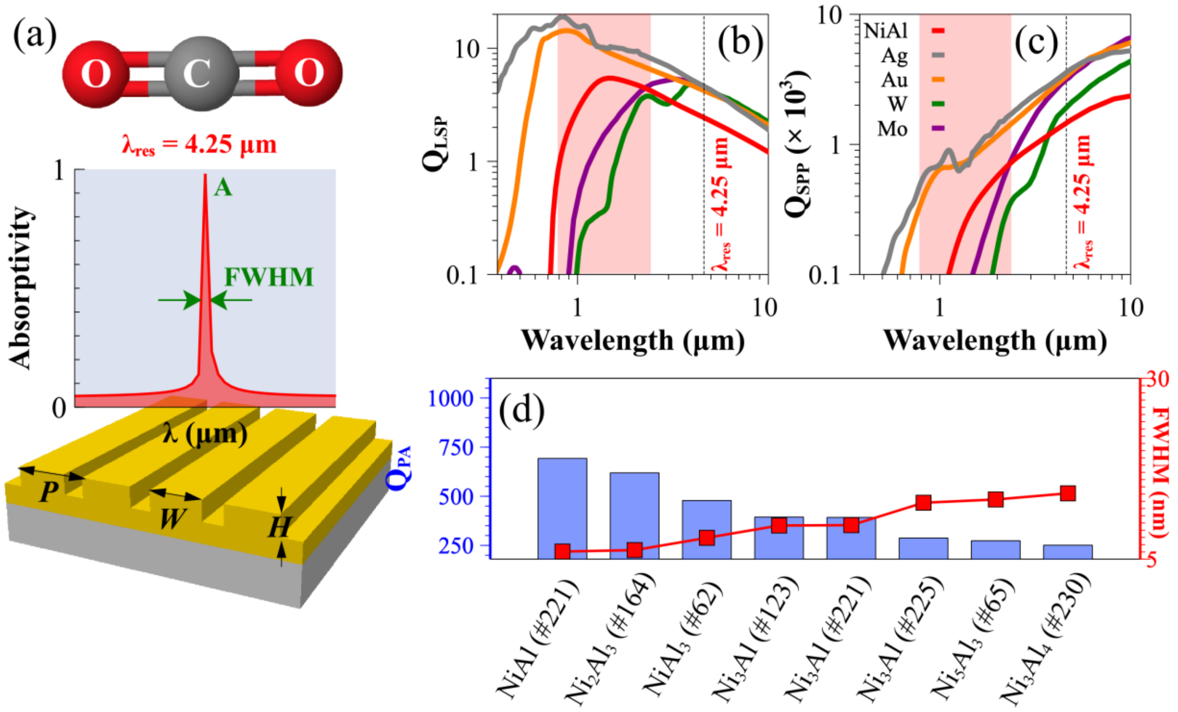

Figure 4. (a) 3D model of the grating configuration and desired absorptivity spectrum peaking at 4.25 μm to match the absorption band of CO_2 gas. Comparison of two FOMs: (b) Q_{LSP} and (c) Q_{SPP} for NiAl and conventional plasmonic materials (Ag, Au, W, and Mo). The red area represents the near-IR region (0.78–2.5 μm) The vertical dashed line indicates the resonant wavelength at 4.25 μm. (d) Quality factors (Q_{PA}) (blue bar plot) and FWHMs (red line plot) of all Ni–Al compounds-based grating devices constructed using the optimal structural parameters.

Notably, the performance of a plasmonic absorber, including its absorptivity and wavelength resolution, is strongly influenced by the inherent optical properties of the materials used in microdevices. To emphasize this effect, we benchmarked not only the candidate Ni–Al intermetallic compounds but also four well-established plasmonic materials (Ag, Au, W, and Mo) as perfect absorbers with a resonant wavelength of 4.25 μm.[59] This wavelength matches the absorption band of CO_2 gas and can be used as an IR light source in nondispersive infrared (NDIR) sensors for CO_2. A simple grating configuration exhibiting Wood's anomaly and the structural parameters *P* (periodicity), *W* (grating width), and *H* (grating height) were set to define the perfect absorbers (**Figure 4(a)**).[60] The thickness of the bottom metallic layer was fixed at 0.2 μm to prevent incident light from passing through the device, thereby maximizing the absorption efficiency. For each grating, a grid search was performed by varying the W and H values until absorptivity peaks were found at 4.25 μm. The simulation domain was set from 3.25 to 5.25 μm around the desired absorptivity peak. We assessed the performance or quality factor of a perfect absorber using **Equation (4)**.

$$Q_{PA} = A \times \frac{\lambda_{res}}{FWHM}. \tag{4}$$

Here, A is absorptivity, λ_{res} is the resonant wavelength (4.25 μm), and $FWHM$ is the full-width at half maximum of the absorptivity peak.

Table 4 displays the *FWHMs* and quality factors (Q_{PA}) of the absorptivity spectra, as well as the optimal geometric parameters, obtained from the grid search of the Ni–Al intermetallic compounds and four well-established plasmonic materials, aimed at 4.25 μm in the grating configuration, for comparison. The materials of the Ni–Al compounds in Table 4 are listed in descending order of their FOMs, as illustrated in Figure 2. The results indicate that the improvement in the optical properties corresponds to a narrower *FWHM* and higher Q-factors.

Table 4. *FWHMs* and Q-factors of the absorptivity spectra, and optimal parameters of Ni–Al intermetallic compounds and conventional plasmonic materials (Ag, Au, W, and Mo) aimed at 4.25 μm in the grating configuration.

Material	Space group	FWHM [nm]	Q_{PA}	P [μm]	W [μm]	H [μm]
Ag	*Fm*-3*m* (#225)	5.70	731.05	4.25	1.46	0.16
Au	*Fm*-3*m* (#225)	5.75	714.34	4.25	1.46	0.16
W	*Im-3m (#229)*	5.35	718.33	4.25	1.13	0.13
Mo	*Im-3m (#229)*	5.60	747.70	4.25	1.46	0.14
NiAl	*Pm*-3*m* (#221)	6.05	692.43	4.25	1.44	0.16
Ni_2Al_3	*P*-3*m*1 (#164)	6.25	618.87	4.25	1.22	0.18
$NiAl_3$	*Pnma* (#62)	7.95	478.51	4.25	1.23	0.23
Ni_3Al	*P*4/*mmm* (#123)	9.65	394.27	4.25	1.14	0.25
Ni_3Al	*Pm*-3*m* (#221)	9.70	392.42	4.25	1.14	0.25
Ni_3Al	*Fm*-3*m* (#225)	12.80	287.70	4.25	1.18	0.25
Ni_5Al_3	*Cmmm* (#65)	13.25	273.90	4.25	1.18	0.25
Ni_3Al_4	*Ia*-3*d* (#230)	14.10	251.07	4.25	1.22	0.25

In **Figure 4(b)** and **4(c)**, we compare the optical properties of NiAl, the best-performing material among the Ni–Al intermetallic compounds, with those of conventional plasmonic materials (Ag, Au, W, and Mo) using common FOMs, Q_{LSP} and Q_{SPP}. Notably, Ag and Au exhibit exceptionally high FOMs, particularly in the visible region. However, in the mid-IR region, the optical properties of NiAl are comparable to those of Ag, Au, W, and Mo.

Specifically, in the near-IR region (0.78–2.5 μm), as indicated by the red area in Figures 4(b) and 4(c), NiAl exhibits higher FOMs compared to W and Mo. According to Wien's law, this wavelength range corresponds to peak blackbody radiation temperatures between approximately 886 °C and 3442 °C. This suggests that heat-resistant NiAl superalloy-based microdevices are suitable for high-performance applications under high-temperature operating conditions. In Table 4, a comparison among the best NiAl-based microdevice and devices constructed using Ag, Au, W, and Mo reveals that the NiAl-based microdevices can achieve a performance equivalent to that of conventional plasmonic materials.

In summary, based on its optical properties and microdevice performance, NiAl, which crystallizes in a CsCl-type structure with the *Pm-3m* (#221) space group, was identified as the best candidate among Ni–Al intermetallic compounds. Furthermore, by benchmarking NiAl-based microdevices against their Ag, Au, W, and Mo counterparts, we assessed the balance between optical performance and practical considerations, such as high-temperature stability, demonstrating their potential as a robust alternative to conventional plasmonic materials.

2.3.2. Proposed NiAl-based microdevices for IR applications

Upon assessing the effects of different materials on the performance of the IR microdevices, NiAl (*Pm*-3*m*, #221) was found to have excellent optical properties and enhanced microdevice performance. Next, we focused on the geometrical optimization of three different microdevice designs using NiAl as the most promising thin-film material for IR photothermal applications with different spectral emission features. The configurations selected for this study included gratings, microtrenches, and metal–insulator–metal (MIM) stripes.[32,61,62] As before, in all microdevices, a NiAl layer with a thickness of 0.2 μm was used as a perfect reflector to prevent the passage of light.

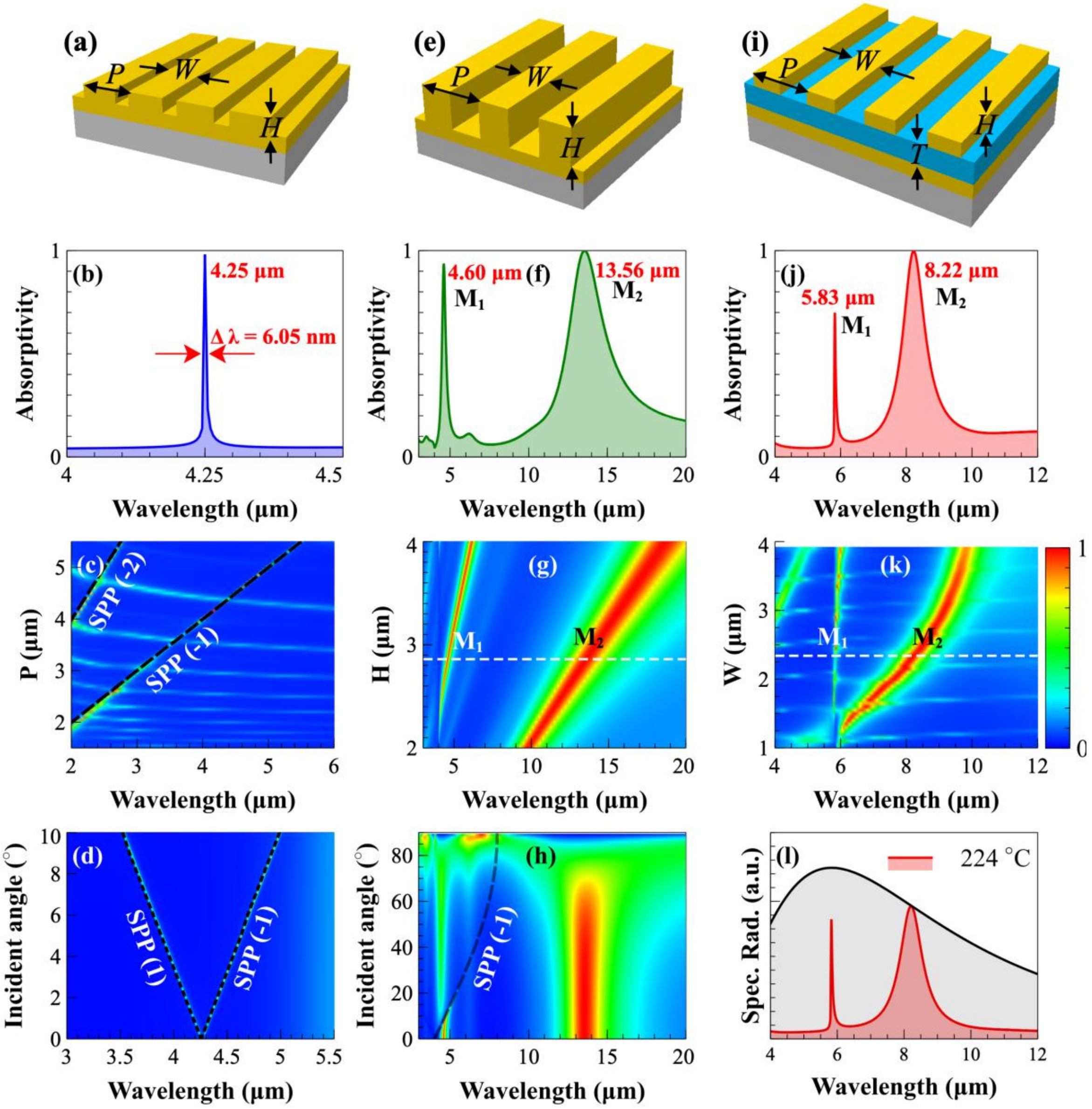

Figure 5. (a) Grating 3D model, (b) absorptivity aimed at 4.25 μm, (c) *P*-dependent, and (d) angle-dependent absorptivity of a NiAl grating. (e) Microtrench 3D model, (f) dual-band absorptivity/emissivity aimed at 4.60 and 13.56 μm, (g) *H*-dependent, (h) angle-dependent absorptivity of a NiAl microtrench configuration. (i) 3D model of MIM stripes (j) dual-band absorptivity aimed at 5.83 and 8.22 μm, (k) *W*-dependent absorptivity, and (l) spectral radiance at 224 °C of this NiAl MIM trench.

Figure 5(a) illustrates the NiAl-based grating and its absorptivity (**Figure 5(b)**) with the optimized structural parameters (Table 3). A narrow *FWHM* of 6.05 nm results in a high Q_{PA} of 692.43, indicating excellent absorption performance. The periodicity-dependent absorptivity in **Figure 5(c)** reveals a linear dependence of the resonant wavelength on the periodicity. At normal incidence, the resonant mode achieves peak absorptivity at 4.25 μm (**Figure 5(d)**). However, the absorption efficiency drops sharply for incident angles above 1°, and the resonant peaks split and shift, indicating strong angle sensitivity, which is ideal for ultrahigh-directivity IR applications. The periodicity-dependent SPP(-1) and SPP(-2) curves in Figure 5(c) and the angular-dependent SPP(-1) and SPP(1) curves in Figure 5(d) originate from surface plasmon polariton (SPP) excitation, explained by the phase-matching condition at the metal-dielectric interface.[32,63,64]

Figure 5(e) illustrates the 3D scheme of a NiAl microtrench with deep trenches. Using P = 4 μm, W = 3.7 μm, and H = 2.86 μm, it achieves two absorption peaks at M_1 = 4.60 μm and M_2 = 13.56 μm with efficiencies of 0.93 and 1.00, respectively (**Figure 5(f)**). The resonant wavelengths depend on H (**Figure 5(g)**), allowing tunability across the mid-IR region for key molecular vibrations. **Figure 5(h)** illustrates the angle-dependent absorptivity. The M_1 mode remains efficient up to 10° and is influenced by SPP(-1), whereas M_2 is angularly insensitive, making it suitable for omnidirectional IR applications. Despite requiring intricate fabrication, its monolithic geometry makes it ideal for ultrahigh-temperature applications such as IR heaters and thermal emitters.

The NiAl-based MIM microstripe array was designed by adding an Al_2O_3 layer between the NiAl metallic mirror and stripe array (**Figure 5(i)**). Optimized structural parameters were P = 5.8 μm, W = 2.34 μm, H = 0.2 μm, and T = 0.2 μm. Similar to the microtrench, it exhibits dual-band resonance at 5.83 μm (M_1) and 8.22 μm (M_2) (**Figure 5(j)**). The influence of W on the absorptivity spectra was examined while keeping P, H, and T constant (**Figure 5(k)**). M_1 remained nearly unchanged, indicating a grating-coupled SPP-like mode, whereas M_2 varied linearly with W and behaved as a localized surface plasmon resonance-like (LSPR) mode. Increasing W widened the spectral separation, allowing flexible tuning of the dual peaks for selective molecular targeting. As a proof of concept, the NiAl MIM microstripe was designed to match acetone's vibrational frequencies at 5.83 μm and 8.22 μm. According to Kirchhoff's law, these dual-band absorbers function as selective thermal emitters upon heating. Unlike blackbody heaters that excite a broad range of molecules, these devices efficiently heat specific molecules by matching their vibrational absorption bands. Notably, the NiAl microstripe at 224 °C exhibits sharp thermal emission at 5.83 μm (**Figure 5(l)**), according to Wien's law formula ($\lambda_{peak} = b/T$, where b = 2.898 mm, K is the Wien's displacement constant, and T is the absolute temperature in K).

We examined three types of NiAl-based microdevices: gratings, microtrenches, and MIM stripes. The grating structure (Figure 5(a)) exhibited a narrow absorptivity band; however, it was highly angle-dependent, making it suitable for high-directivity applications such as NDIR gas sensors, but unsuitable for omnidirectional applications. To address this limitation, the microtrench structure (Figure 5(f)) offers dual-band absorption, with the M_2 mode being angle-insensitive, and its peak remaining stable regardless of the incident angle (Figure 5(h)). The resonant wavelength was also tunable by varying H (Figure 5(g)), although longer wavelengths increased the fabrication time and cost. The MIM microstripe device (Figure 5(i)) allowed precise tuning of structural parameters, such as a NiAl stripe as thin as 0.2 µm, reducing deposition and etching times. In summary, different NiAl metasurface designs and resonant modes can be optimized for various IR applications based on specific requirements.

3. Conclusions

In this study, we integrated DFT and electromagnetic simulations to optimize the chemical composition of Ni–Al intermetallic compounds and the device geometry for IR photothermal absorbers/emitters. First, we explored the correlation between the crystal structure and optical properties of the Ni–Al intermetallic compounds. Our findings revealed that NiAl, a high-temperature superalloy, exhibits excellent optical properties on par with conventional plasmonic materials in the IR region. The measured structural parameters, electrical characteristics, and optical properties of the single-crystal NiAl sample were consistent with the predicted results, confirming the accuracy and effectiveness of the proposed approach for predicting the optical properties in the IR region. Second, an examination of the relationship between the performance of the absorber/emitter devices and the constituent Ni–Al intermetallic compounds revealed that the best candidate material, NiAl, exhibited excellent microdevice performance, potentially achieving an excellent quality factor of 692. NiAl has emerged as a novel high-temperature material in the IR region owing to its thermal stability and excellent plasmonic properties. As a proof of concept, we designed NiAl-based metasurfaces with gratings, microtrenches, and MIM microstripe structures. The proposed microdevices exhibited resonances with narrowband near-perfect absorptivity, covering a broad spectrum in the mid-IR region. Therefore, these thermophotonic microdevices have various potential applications, such as in highly sensitive IR sensors/detectors, surface-enhanced infrared absorption (SEIRA), and thermal emitters for heaters and thermophotovoltaic applications. In the long term, our research aims to bridge theoretical and simulation studies with experimental advancements in superalloy-based thermophotonic devices. We adopted a stepwise approach, beginning with theoretical studies, followed by the successful uniaxial and smooth surface preparation of NiAl thin films and the fabrication of NiAl-based microdevices. Additionally, key fabrication challenges such as precise etching techniques for structuring NiAl metasurfaces are being actively addressed to ensure the feasibility of high-performance thermophotonic applications.

4. Experimental Section

4.1. First-principles DFT calculations

DFT calculations were performed using the Vienna ab initio Simulation Package (VASP) code with projector-augmented wave (PAW) pseudopotentials and the Perdew–Burke–Ernzerhof (PBE) generalized gradient approximation (GGA) functional.[33][34][35] The energy cutoff was set to 520 eV for all the calculations. The total energy convergence was set to 10^{-6} eV atom^{-1}. The lattice constants were fully relaxed until the residual force was less than 0.005 eV Å^{-1}. The Monkhorst–Pack scheme,[36] having reciprocal space resolutions of 2π × 0.02 and 2π × 0.006 Å^{-1}, were set for structural optimization and optical calculations, respectively. The smearing width was set to 0.1 eV. We used the Drude-Lorentz model for optical calculations and ellipsometry fitting of the NiAl single crystal. The dielectric function of the metal is a combination of the interband and intraband components:

$$\varepsilon(\omega) = \varepsilon^{inter}(\omega) + \varepsilon^{intra}(\omega). \qquad (1)$$

The interband dielectric function (Lorentz part) was calculated using independent particle approximation (IPA),[37] as implemented in the VASP code. The intraband dielectric function is obtained from the Drude expression

$$\varepsilon_{intra}(\omega) = 1 - \frac{\omega_p^2}{\omega^2 + i\Gamma_D\omega}, \qquad (2)$$

where ω_p and Γ_D are the plasma frequency and Drude scattering rate, respectively.

The plasma frequency (ω_p) was calculated from the band structure as follows:[38]

$$\omega_P^2(\alpha,\beta) = -\frac{4\pi e^2}{V}\sum_{nk} 2\frac{\partial f(E_n)}{\partial E_n}\langle e_\alpha \frac{\partial E_{nk}}{\partial k}\rangle \langle e_\beta \frac{\partial E_{nk}}{\partial k}\rangle, \qquad (3)$$

where e is the electron charge, V is the cell volume, E_{nk} is the band energy for the n-th band at k-points k, f represents the occupation number for band n, and e_α and e_β denote the unit vectors in the Cartesian space. In the IR region, the scattering rate was roughly chosen as an empirical parameter at $\Gamma_D = 0.1$ eV.[32,39] To select a suitable functional for comparison with the experimental optical properties in the IR region, the DFT + U formalism (U = 6.4 eV was applied to the d-electrons of nickel to improve the exchange correlation and compared with the PBE results.[40,41]

4.2. Electromagnetic simulations

The optical spectral absorptivity of the microdevices was simulated using a Rigorous Coupled-Wave Analysis (RCWA) method implemented in the DiffractMOD package (Synopsys RSoft Photonic Device Tools).

4.3. Material characterization

The theoretical results for NiAl (Pm-$3m$, #221) were compared with the experimental data to examine the accuracy of the simulation method. Single-crystal NiAl was characterized to determine its lattice constant, dielectric function, and electrical conductivity. The cubic lattice constant of NiAl (denoted as a) was calculated using X-ray diffraction (XRD; Rigaku Smartlab X-ray Diffractometer, Japan). The frequency-dependent dielectric function $\varepsilon(\omega)$ of NiAl single crystal was obtained by spectroscopic ellipsometry. The FTIR spectroscopic ellipsometers SENTECH (UV–Near-IR) and SENDIRA (Mid-IR) were used for measurements in the spectral region of interest (0.2–25 μm). The Drude-Lorentz model, which combines the Drude expression of free charge carriers (Equation (2)) and Lorentz oscillators, was used for the ellipsometry fitting. Once the plasma frequency (ω_p) and scattering rate (Γ_D) were estimated from Ellipsometry fitting via Drude-Lorentz model, the electrical conductivity (σ) was calculated as $\sigma(cm^{-1}) = \omega_p^2/(4\pi\Gamma_D)$. The observed structural parameters and the electrical and optical properties of the single-crystal NiAl are listed in Table 3.

Acknowledgements

This study was supported by KAKENHI (Grant No. 16H06364). DFT calculations were performed using a Numerical Material Simulator at the National Institute for Materials Science (NIMS). We are grateful to M. Kitajima and S. Otani for the fruitful discussions.

Received: ((will be filled in by the editorial staff))
Revised: ((will be filled in by the editorial staff))
Published online: ((will be filled in by the editorial staff))

References

[1] N. Yu, F. Capasso, *Nat. Mater.* **2014**, *13*, 139, https://doi.org/10.1038/nmat3839.
[2] M.W. Knight, N.S. King, L. Liu, H.O. Everitt, P. Nordlander, N.J. Halas, *ACS Nano* **2014**, *8*, 834, https://doi.org/10.1021/nn405495q.
[3] T.D. Dao, C.V. Hoang, N. Nishio, N. Yamamoto, A. Ohi, T. Nabatame, M. Aono, T. Nagao, *Micromachines* **2019**, *10*, 468, https://doi.org/10.3390/mi10070468.
[4] M. Hasegawa, *J. Phys. Soc. Jpn.* **1971**, *31*, 649, https://doi.org/10.1143/JPSJ.31.649.
[5] K. Utsumi, S. Ichimaru, *Phys. Rev. B* **1981**, *23*, 3291, https://doi.org/10.1103/PhysRevB.23.3291.
[6] T. Nagao, T. Hildebrandt, M. Henzler, S. Hasegawa, *Phys. Rev. Lett.* **2001**, *86*, 5747, https://doi.org/10.1103/PhysRevLett.86.5747.
[7] S.C. Deevi, V.K. Sikka, *Intermetallics* **1996**, *4*, 357, https://doi.org/10.1016/0966-9795(95)00056-9.
[8] Y. Koizumi, H. Harada, T. Yokokawa, T. Kobayashi, US8852500B2, **2014**.
[9] R. Darolia, *JOM* **1991**, *43*, 44, https://doi.org/10.1007/BF03220163.
[10] J. Salem, R. Noebe, D.R. Wheeler, F. Holland, J. Palko, S. Duffy, P.K. Wright, Reliability analysis of single crystal NiAl turbine blades, https://ntrs.nasa.gov/citations/19960007500, accessed: December, **2023**.
[11] R. Darolia, *Intermetallics* **2000**, *8*, 1321, https://doi.org/10.1016/S0966-9795(00)00081-9.
[12] D.B. Miracle, *Acta Metall. Mater.* **1993**, *41*, 649, https://doi.org/10.1016/0956-7151(93)90001-9.
[13] Y. Yamaguchi, T. Aoki, J.O. Brittain, *J. Phys. Chem. Solids* **1970**, *31*, 1325, https://doi.org/10.1016/0022-3697(70)90137-X.
[14] D. Shi, B. Wen, R. Melnik, S. Yao, T. Li, *J. Solid State Chem.* **2009**, *182*, 2664, https://doi.org/10.1016/j.jssc.2009.07.026.
[15] L. Mo, X. Zhou, X. Liu, M. Zhan, Y.-J. Zhao, J. Du, *J. Mater. Res. Technol.* **2023**, *24*, 6227, https://doi.org/10.1016/j.jmrt.2023.04.168.
[16] H. Fu, D. Li, F. Peng, T. Gao, X. Cheng, *Comput. Mater. Sci.* **2008**, *44*, 774, https://doi.org/10.1016/j.commatsci.2008.05.026.
[17] I. Ansara, N. Dupin, H.L. Lukas, B. Sundman, *J. Alloys Compd.* **1997**, *247*, 20, https://doi.org/10.1016/S0925-8388(96)02652-7.
[18] K. Rzyman, Z. Moser, R.E. Watson, M. Weinert, *J. Phase Equilibria* **1998**, *19*, 106, https://doi.org/10.1361/105497198770342562.
[19] J.J. Rechtien, C.R. Kannewurf, J.O. Brittain, *J. Appl. Phys.* **2004**, *38*, 3045, https://doi.org/10.1063/1.1710060.
[20] K.J. Kim, B.N. Harmon, D.W. Lynch, *Phys. Rev. B* **1991**, *43*, 1948, https://doi.org/10.1103/PhysRevB.43.1948.
[21] G. Mondio, A.D. Laine, A.M. Mezzasalma, G. Cubiotti, Yu.N. Kucherenko, *J. Electron Spectrosc. Relat. Phenom.* **1997**, *85*, 1, https://doi.org/10.1016/S0368-2048(97)00019-4.
[22] J.Y. Rhee, B.N. Harmon, D.W. Lynch, *Phys. Rev. B* **1997**, *55*, 4124, https://doi.org/10.1103/PhysRevB.55.4124.

[23] R. Saniz, L.-H. Ye, T. Shishidou, A.J. Freeman, *Phys. Rev. B* **2006**, *74*, 014209, https://doi.org/10.1103/PhysRevB.74.014209.

[24] Sasovskaya I. I., Korabel V. P., Shreder E. I., *Phys. Status Solidi B* **1985**, *129*, 667, https://doi.org/10.1002/pssb.2221290226.

[25] Egorushkin V. E., Kul'mentyev A. I., Rubin P. E., *Solid State Commun.* **1986**, *57*, 821, https://doi.org/10.1016/0038-1098(86)90184-5.

[26] K. Schlemper, L.K. Thomas, *Phys. Rev. B* **1994**, *50*, 17802, https://doi.org/10.1103/PhysRevB.50.17802.

[27] R. Darolia, W.S. Walston, R. Noebe, A. Garg, B.F. Oliver, *Intermetallics* **1999**, *7*, 1195, https://doi.org/10.1016/S0966-9795(99)00043-6.

[28] D. Zhong, J.J. Moore, J. Disam, S. Thiel, I. Dahan, *Surf. Coat. Technol.* **1999**, *120*, 22, https://doi.org/10.1016/S0257-8972(99)00334-5.

[29] A. Hibino, S. Matsuoka, M. Kiuchi, *J. Mater. Process. Technol.* **2001**, *112*, 127, https://doi.org/10.1016/S0924-0136(01)00558-1.

[30] P.T. Tran, H.D. Ngo, T.D. Ngo, T. Nagao, *Appl. Phys. Express* **2021**, *14*, 087001, https://doi.org/10.35848/1882-0786/ac0ecd.

[31] T.D. Ngo, T.D. Dao, N.T. Cuong, N. Umezawa, T. Nagao, *Phys. Rev. Mater.* **2020**, *4*, 055201, https://doi.org/10.1103/PhysRevMaterials.4.055201.

[32] T.D. Ngo, T.P. Tran, H.D. Ngo, T. Nagao, *Adv. Opt. Mater.* **2022**, *10*, 2201320, https://doi.org/10.1002/adom.202201320.

[33] G. Kresse, J. Furthmüller, *Phys. Rev. B* **1996**, *54*, 11169, https://doi.org/10.1103/PhysRevB.54.11169.

[34] P.E. Blöchl, *Phys. Rev. B* **1994**, *50*, 17953, https://doi.org/10.1103/PhysRevB.50.17953.

[35] J.P. Perdew, K. Burke, M. Ernzerhof, *Phys. Rev. Lett.* **1996**, *77*, 3865, https://doi.org/10.1103/PhysRevLett.77.3865.

[36] J.D. Pack, H.J. Monkhorst, *Phys. Rev. B* **1977**, *16*, 1748, https://doi.org/10.1103/PhysRevB.16.1748.

[37] M. Gajdoš, K. Hummer, G. Kresse, J. Furthmüller, F. Bechstedt, *Phys. Rev. B* **2006**, *73*, 045112, https://doi.org/10.1103/PhysRevB.73.045112.

[38] Judith Harl, *Master Thesis*, University of Vienna **2008**.

[39] P.R. West, S. Ishii, G.V. Naik, N.K. Emani, V.M. Shalaev, A. Boltasseva, *Laser Photonics Rev.* **2010**, *4*, 795, https://doi.org/10.1002/lpor.200900055.

[40] S.L. Dudarev, G.A. Botton, S.Y. Savrasov, C.J. Humphreys, A.P. Sutton, *Phys. Rev. B* **1998**, *57*, 1505, https://doi.org/10.1103/PhysRevB.57.1505.

[41] L. Wang, T. Maxisch, G. Ceder, *Phys. Rev. B* **2006**, *73*, 195107, https://doi.org/10.1103/PhysRevB.73.195107.

[42] G. Bergerhoff, I.D. Brown, *Crystallographic Databases*, Chester, UK, **1987**.

[43] D. Zagorac, H. Müller, S. Ruehl, J. Zagorac, S. Rehme, *J. Appl. Crystallogr.* **2019**, *52*, 918, https://doi.org/10.1107/S160057671900997X.

[44] Materials Data on AlNi3 by Materials Project, Lawrence Berkeley National Lab. (LBNL), Berkeley, CA. LBNL Materials Project, **2020**. https://doi.org/10.17188/1281790.

[45] B.I. Min, A.J. Freeman, H.J.F. Jansen, Phys. Rev. B **1988**, *37*, 6757, https://doi.org/10.1103/PhysRevB.37.6757.

[46] J.O. Conway, T.J. Prior, *J. Alloys Compd.* **2019**, *774*, 69, https://doi.org/10.1016/j.jallcom.2018.09.307.

[47] C. Didier, W.K. Pang, Z. Guo, S. Schmid, V.K. Peterson, *Chem. Mater.* **2020**, *32*, 2518, https://doi.org/10.1021/acs.chemmater.9b05145.

[48] N. Belyavina, V. Markiv, O. Nakonechna, F. Lozovyi, *J. Alloys Compd.* **2014**, *593*, 41, https://doi.org/10.1016/j.jallcom.2014.01.073.

[49] F.A. Ainutdinov, S.K. Khairidinov, A.V. Vakhobov, *SSR* **1987**, *30*, 169.
[50] K.H. Han, W.K. Choo, Scr. Metall. **1983**, *17*, 281, https://doi.org/10.1016/0036-9748(83)90157-6.
[51] M. Ellner, S. Kek, B. Predel, *J. Common Met.* **1989**, *154*, 207, https://doi.org/10.1016/0022-5088(89)90185-9.
[52] A.D. Rakić, A.B. Djurišić, J.M. Elazar, M.L. Majewski, *Appl. Opt.* **1998**, *37*, 5271, https://doi.org/10.1364/AO.37.005271.
[53] M. Kumar, N. Umezawa, S. Ishii, T. Nagao, *ACS Photonics* **2016**, *3*, 43, https://doi.org/10.1021/acsphotonics.5b00409.
[54] J. Heyd, G.E. Scuseria, M. Ernzerhof, *J. Chem. Phys.* **2003**, *118*, 8207, https://doi.org/10.1063/1.1564060.
[55] J. Heyd, G.E. Scuseria, M. Ernzerhof, *J. Chem. Phys.* **2006**, *124*, 219906, https://doi.org/10.1063/1.2204597.
[56] L. Hedin, *J. Phys. Condens. Matter* **1999**, *11*, R489, https://doi.org/10.1088/0953-8984/11/42/201.
[57] Z. Tong, S. Li, X. Ruan, H. Bao, *Phys. Rev. B* **2019**, *100*, 144306, https://doi.org/10.1103/PhysRevB.100.144306.
[58] G. Kirchhoff, *Ann. Phys.* **1860**, *185*, 275, https://doi.org/10.1002/andp.18601850205.
[59] E.D. Palik, ed., Handbook of optical constants of solids, Academic Press, New York, 1998.
[60] T.D. Dao, S. Ishii, A.T. Doan, Y. Wada, A. Ohi, T. Nabatame, T. Nagao, *Adv. Sci.* **2019**, *6*, 1900579, https://doi.org/10.1002/advs.201900579.
[61] P.T. Tran, T.D. Ngo, H.D. Ngo, Ø.S. Handegård, T. Nagao, *Opt. Express* **2022**, *30*, 38630, https://doi.org/10.1364/OE.463522.
[62] R.P. Sugavaneshwar, Ø.S. Handegård, A.T. Doan, T.D. Ngo, T.P. Tran, H.D. Ngo, T.D. Dao, S. Ishii, S. Otani, T. Nagao, *Adv. Opt. Mater.* **2022**, *10*, 2101787, https://doi.org/10.1002/adom.202101787.
[63] S.A. Maier, *Plasmonics: fundamentals and applications*, Springer, NY, **2007**.
[64] J.R. Sambles, G.W. Bradbery, F. Yang, *Contemp. Phys.* **1991**, *32*, 173, https://doi.org/10.1080/00107519108211048.

[1] N. Yu, F. Capasso, Flat optics with designer metasurfaces, Nat. Mater. 13 (2014) 139–150. https://doi.org/10.1038/nmat3839.
[2] M.W. Knight, N.S. King, L. Liu, H.O. Everitt, P. Nordlander, N.J. Halas, Aluminum for Plasmonics, ACS Nano 8 (2014) 834–840. https://doi.org/10.1021/nn405495q.
[3] T.D. Dao, C.V. Hoang, N. Nishio, N. Yamamoto, A. Ohi, T. Nabatame, M. Aono, T. Nagao, Dark-Field Scattering and Local SERS Mapping from Plasmonic Aluminum Bowtie Antenna Array, Micromachines 10 (2019) 468. https://doi.org/10.3390/mi10070468.
[4] M. Hasegawa, Theory of Plasmon Damping in Metals. II. Effects of Electron-Ion Interaction, J. Phys. Soc. Jpn. 31 (1971) 649–667. https://doi.org/10.1143/JPSJ.31.649.
[5] K. Utsumi, S. Ichimaru, Dielectric formulation of strongly coupled electron liquid at metallic densities. III. Dynamic structure factor, Phys. Rev. B 23 (1981) 3291–3300. https://doi.org/10.1103/PhysRevB.23.3291.
[6] T. Nagao, T. Hildebrandt, M. Henzler, S. Hasegawa, Dispersion and Damping of a Two-Dimensional Plasmon in a Metallic Surface-State Band, Phys. Rev. Lett. 86 (2001) 5747–5750. https://doi.org/10.1103/PhysRevLett.86.5747.

[7] S.C. Deevi, V.K. Sikka, Nickel and iron aluminides: an overview on properties, processing, and applications, Intermetallics 4 (1996) 357–375. https://doi.org/10.1016/0966-9795(95)00056-9.

[8] Y. Koizumi, H. Harada, T. Yokokawa, T. Kobayashi, Ni-base superalloy, method for producing the same, and turbine blade or turbine vane components, US8852500B2, 2014. https://patents.google.com/patent/US8852500/en (accessed January 4, 2024).

[9] R. Darolia, NiAl alloys for high-temperature structural applications, JOM 43 (1991) 44–49. https://doi.org/10.1007/BF03220163.

[10] J. Salem, R. Noebe, D.R. Wheeler, F. Holland, J. Palko, S. Duffy, P.K. Wright, Reliability analysis of single crystal NiAl turbine blades, 1995. https://ntrs.nasa.gov/citations/19960007500 (accessed December 22, 2023).

[11] R. Darolia, Ductility and fracture toughness issues related to implementation of NiAl for gas turbine applications, Intermetallics 8 (2000) 1321–1327. https://doi.org/10.1016/S0966-9795(00)00081-9.

[12] D.B. Miracle, Overview No. 104 The physical and mechanical properties of NiAl, Acta Metall. Mater. 41 (1993) 649–684. https://doi.org/10.1016/0956-7151(93)90001-9.

[13] Y. Yamaguchi, T. Aoki, J.O. Brittain, Electronic structure of β′-NiAl, J. Phys. Chem. Solids 31 (1970) 1325–1343. https://doi.org/10.1016/0022-3697(70)90137-X.

[14] D. Shi, B. Wen, R. Melnik, S. Yao, T. Li, First-principles studies of Al–Ni intermetallic compounds, J. Solid State Chem. 182 (2009) 2664–2669. https://doi.org/10.1016/j.jssc.2009.07.026.

[15] L. Mo, X. Zhou, X. Liu, M. Zhan, Y.-J. Zhao, J. Du, Microstructure and thermal-physical properties of hypereutectic Al-Ni alloys, J. Mater. Res. Technol. 24 (2023) 6227–6237. https://doi.org/10.1016/j.jmrt.2023.04.168.

[16] H. Fu, D. Li, F. Peng, T. Gao, X. Cheng, Ab initio calculations of elastic constants and thermodynamic properties of NiAl under high pressures, Comput. Mater. Sci. 44 (2008) 774–778. https://doi.org/10.1016/j.commatsci.2008.05.026.

[17] I. Ansara, N. Dupin, H.L. Lukas, B. Sundman, Thermodynamic assessment of the Al-Ni system, J. Alloys Compd. 247 (1997) 20–30. https://doi.org/10.1016/S0925-8388(96)02652-7.

[18] K. Rzyman, Z. Moser, R.E. Watson, M. Weinert, Enthalpies of formation of AlNi: Experiment versus theory, J. Phase Equilibria 19 (1998) 106–111. https://doi.org/10.1361/105497198770342562.

[19] J.J. Rechtien, C.R. Kannewurf, J.O. Brittain, Optical Constants of β-Phase NiAl, J. Appl. Phys. 38 (2004) 3045–3050. https://doi.org/10.1063/1.1710060.

[20] K.J. Kim, B.N. Harmon, D.W. Lynch, Calculation of the optical spectra of β’-NiAl and CoAl, Phys. Rev. B 43 (1991) 1948–1953. https://doi.org/10.1103/PhysRevB.43.1948.

[21] G. Mondio, A.D. Laine, A.M. Mezzasalma, G. Cubiotti, Yu.N. Kucherenko, The reflectivity spectra of Al3Ni and AlNi3, J. Electron Spectrosc. Relat. Phenom. 85 (1997) 1–7. https://doi.org/10.1016/S0368-2048(97)00019-4.

[22] J.Y. Rhee, B.N. Harmon, D.W. Lynch, Optical properties and electronic structures of Ni3Al alloys, Phys. Rev. B 55 (1997) 4124–4128. https://doi.org/10.1103/PhysRevB.55.4124.

[23] R. Saniz, L.-H. Ye, T. Shishidou, A.J. Freeman, Structural, electronic, and optical properties of NiAl3: First-principles calculations, Phys. Rev. B 74 (2006) 014209. https://doi.org/10.1103/PhysRevB.74.014209.

[24] Sasovskaya I. I., Korabel V. P., Shreder E. I., Optical Properties of NiAl Intermetallic Compounds during Concentration and Temperature B.C.C.–F.C.T. Transitions, Phys. Status Solidi B 129 (1985) 667–674. https://doi.org/10.1002/pssb.2221290226.

[25] Egorushkin V. E., Kul'mentyev A. I., Rubin P. E., Electron structure and optical properties of Ni-Al, Solid State Commun. 57 (1986) 821–823. https://doi.org/10.1016/0038-1098(86)90184-5.

[26] K. Schlemper, L.K. Thomas, Optical properties and electronic structure of the intermetallic phases NiAl, CoAl, and FeAl, Phys. Rev. B 50 (1994) 17802–17810. https://doi.org/10.1103/PhysRevB.50.17802.

[27] R. Darolia, W.S. Walston, R. Noebe, A. Garg, B.F. Oliver, Mechanical properties of high purity single crystal NiAl, Intermetallics 7 (1999) 1195–1202. https://doi.org/10.1016/S0966-9795(99)00043-6.

[28] D. Zhong, J.J. Moore, J. Disam, S. Thiel, I. Dahan, Deposition of NiAl thin films from NiAl compound target fabricated via combustion synthesis, Surf. Coat. Technol. 120–121 (1999) 22–27. https://doi.org/10.1016/S0257-8972(99)00334-5.

[29] A. Hibino, S. Matsuoka, M. Kiuchi, Synthesis and sintering of Ni3Al intermetallic compound by combustion synthesis process, J. Mater. Process. Technol. 112 (2001) 127–135. https://doi.org/10.1016/S0924-0136(01)00558-1.

[30] P.T. Tran, H.D. Ngo, T.D. Ngo, T. Nagao, Uniaxially oriented nickel aluminum superalloy films sputtered with in situ heating, Appl. Phys. Express 14 (2021) 087001. https://doi.org/10.35848/1882-0786/ac0ecd.

[31] T.D. Ngo, T.D. Dao, N.T. Cuong, N. Umezawa, T. Nagao, Combined first-principles and electromagnetic simulation study of n-type doped anatase TiO2 for the applications in infrared surface plasmon photonics, Phys. Rev. Mater. 4 (2020) 055201. https://doi.org/10.1103/PhysRevMaterials.4.055201.

[32] T.D. Ngo, T.P. Tran, H.D. Ngo, T. Nagao, A Simultaneous Material-Device Optimization for Plasmonic Devices: A Combined Ab Initio and Electromagnetic Simulation for Photothermal Transducers, Adv. Opt. Mater. 10 (2022) 2201320. https://doi.org/10.1002/adom.202201320.

[33] G. Kresse, J. Furthmüller, Efficient iterative schemes for ab initio total-energy calculations using a plane-wave basis set, Phys. Rev. B 54 (1996) 11169–11186. https://doi.org/10.1103/PhysRevB.54.11169.

[34] P.E. Blöchl, Projector augmented-wave method, Phys. Rev. B 50 (1994) 17953–17979. https://doi.org/10.1103/PhysRevB.50.17953.

[35] J.P. Perdew, K. Burke, M. Ernzerhof, Generalized Gradient Approximation Made Simple, Phys. Rev. Lett. 77 (1996) 3865–3868. https://doi.org/10.1103/PhysRevLett.77.3865.

[36] J.D. Pack, H.J. Monkhorst, "Special points for Brillouin-zone integrations"—a reply, Phys. Rev. B 16 (1977) 1748–1749. https://doi.org/10.1103/PhysRevB.16.1748.

[37] M. Gajdoš, K. Hummer, G. Kresse, J. Furthmüller, F. Bechstedt, Linear optical properties in the projector-augmented wave methodology, Phys. Rev. B 73 (2006) 045112. https://doi.org/10.1103/PhysRevB.73.045112.

[38] Judith Harl, Linear response function in density functional theory: Optical spectra and improved description of the electron correlation, University of Vienna, 2008.

[39] P.R. West, S. Ishii, G.V. Naik, N.K. Emani, V.M. Shalaev, A. Boltasseva, Searching for better plasmonic materials, Laser Photonics Rev. 4 (2010) 795–808. https://doi.org/10.1002/lpor.200900055.

[40] S.L. Dudarev, G.A. Botton, S.Y. Savrasov, C.J. Humphreys, A.P. Sutton, Electron-energy-loss spectra and the structural stability of nickel oxide: An LSDA+U study, Phys. Rev. B 57 (1998) 1505–1509. https://doi.org/10.1103/PhysRevB.57.1505.

[41] L. Wang, T. Maxisch, G. Ceder, Oxidation energies of transition metal oxides within the GGA + U framework, Phys. Rev. B 73 (2006) 195107. https://doi.org/10.1103/PhysRevB.73.195107.

[42] G. Bergerhoff, I.D. Brown, Crystallographic Databases, International Union of Crystallography, Chester, UK, 1987.

[43] D. Zagorac, H. Müller, S. Ruehl, J. Zagorac, S. Rehme, Recent developments in the Inorganic Crystal Structure Database: theoretical crystal structure data and related features, J. Appl. Crystallogr. 52 (2019) 918–925. https://doi.org/10.1107/S160057671900997X.

[44] Materials Data on AlNi3 by Materials Project, Lawrence Berkeley National Lab. (LBNL), Berkeley, CA (United States). LBNL Materials Project, 2020. https://doi.org/10.17188/1281790.

[45] B.I. Min, A.J. Freeman, H.J.F. Jansen, Magnetism, electronic structure, and Fermi surface of Ni3Al, Phys. Rev. B 37 (1988) 6757–6762. https://doi.org/10.1103/PhysRevB.37.6757.

[46] J.O. Conway, T.J. Prior, Interstitial nitrides revisited – A simple synthesis of MxMo3N (M = Fe, Co, Ni), J. Alloys Compd. 774 (2019) 69–74. https://doi.org/10.1016/j.jallcom.2018.09.307.

[47] C. Didier, W.K. Pang, Z. Guo, S. Schmid, V.K. Peterson, Phase Evolution and Intermittent Disorder in Electrochemically Lithiated Graphite Determined Using in Operando Neutron Diffraction, Chem. Mater. 32 (2020) 2518–2531. https://doi.org/10.1021/acs.chemmater.9b05145.

[48] N. Belyavina, V. Markiv, O. Nakonechna, F. Lozovyi, Phase equilibria in the Ni–Al–Ga system at 700°C, J. Alloys Compd. 593 (2014) 41–49. https://doi.org/10.1016/j.jallcom.2014.01.073.

[49] F.A. Ainutdinov, S.K. Khairidinov, A.V. Vakhobov, Phase diagram of Aluminium-Barium-Nickel system, Dokl. Akad. Nauk Tadzhikskoi SSR 30 (1987) 169–172.

[50] K.H. Han, W.K. Choo, Carbon effect on ordering of γ′-Ni3Al in rapidly solidified Ni3Al-C alloys, Scr. Metall. 17 (1983) 281–284. https://doi.org/10.1016/0036-9748(83)90157-6.

[51] M. Ellner, S. Kek, B. Predel, Ni3Al4 — A phase with ordered vacancies isotypic to Ni3Ga4, J. Common Met. 154 (1989) 207–215. https://doi.org/10.1016/0022-5088(89)90185-9.

[52] A.D. Rakić, A.B. Djurišić, J.M. Elazar, M.L. Majewski, Optical properties of metallic films for vertical-cavity optoelectronic devices, Appl. Opt. 37 (1998) 5271–5283. https://doi.org/10.1364/AO.37.005271.

[53] M. Kumar, N. Umezawa, S. Ishii, T. Nagao, Examining the Performance of Refractory Conductive Ceramics as Plasmonic Materials: A Theoretical Approach, ACS Photonics 3 (2016) 43–50. https://doi.org/10.1021/acsphotonics.5b00409.

[54] J. Heyd, G.E. Scuseria, M. Ernzerhof, Hybrid functionals based on a screened Coulomb potential, J. Chem. Phys. 118 (2003) 8207–8215. https://doi.org/10.1063/1.1564060.

[55] J. Heyd, G.E. Scuseria, M. Ernzerhof, Erratum: “Hybrid functionals based on a screened Coulomb potential” [J. Chem. Phys. 118, 8207 (2003)], J. Chem. Phys. 124 (2006) 219906. https://doi.org/10.1063/1.2204597.

[56] L. Hedin, On correlation effects in electron spectroscopies and the *GW* approximation, J. Phys. Condens. Matter 11 (1999) R489–R528. https://doi.org/10.1088/0953-8984/11/42/201.

[57] Z. Tong, S. Li, X. Ruan, H. Bao, Comprehensive first-principles analysis of phonon thermal conductivity and electron-phonon coupling in different metals, Phys. Rev. B 100 (2019) 144306. https://doi.org/10.1103/PhysRevB.100.144306.

[58] G. Kirchhoff, Ueber das Verhältniss zwischen dem Emissionsvermögen und dem Absorptionsvermögen der Körper für Wärme und Licht [On the relationship between

the emissivity and absorptivity of a body for heat and light], Ann. Phys. 185 (1860) 275–301. https://doi.org/10.1002/andp.18601850205.

[59] E.D. Palik, ed., Handbook of optical constants of solids, Academic Press, New York, 1998.

[60] T.D. Dao, S. Ishii, A.T. Doan, Y. Wada, A. Ohi, T. Nabatame, T. Nagao, An On-Chip Quad-Wavelength Pyroelectric Sensor for Spectroscopic Infrared Sensing, Adv. Sci. 6 (2019) 1900579. https://doi.org/10.1002/advs.201900579.

[61] P.T. Tran, T.D. Ngo, H.D. Ngo, Ø.S. Handegård, T. Nagao, Metal-insulator-metal strip spectroscopic infrared photothermal absorber based on uniaxially oriented plasmonic lanthanum hexaboride films, Opt. Express 30 (2022) 38630. https://doi.org/10.1364/OE.463522.

[62] R.P. Sugavaneshwar, Ø.S. Handegård, A.T. Doan, T.D. Ngo, T.P. Tran, H.D. Ngo, T.D. Dao, S. Ishii, S. Otani, T. Nagao, Optical Properties and Optimization of LaB6 Thin Films for Photothermal Applications, Adv. Opt. Mater. 10 (2022) 2101787. https://doi.org/10.1002/adom.202101787.

[63] S.A. Maier, Plasmonics: fundamentals and applications, Springer, New York, 2007.

[64] J.R. Sambles, G.W. Bradbery, F. Yang, Optical excitation of surface plasmons: An introduction, Contemp. Phys. 32 (1991) 173–183. https://doi.org/10.1080/00107519108211048.

The table of contents entry should be 50–60 words long and should be written in the present tense. The text should be different from the abstract text.

T. D. Ngo*, H. D. Ngo, T. P. Tran, H. Harada, T. Nagao*

Infrared Thermophotonics: Theoretical benchmarking of Ni–Al superalloys

ToC figure ((Please choose one size: 55 mm broad × 50 mm high **or** 110 mm broad × 20 mm high. Please do not use any other dimensions))